As-built fracture toughness of Ti6Al4V produced by laser powder bed fusion

Danie Louw [1,2], *Melody* Neaves[2], *Thorsten* Becker[3]

[1*] National Laser Center, Council for Scientific and Industrial Research, South Africa, dlouw@csir.co.za
[2] Materials Engineering Research Group, Stellenbosch University, South Africa, melzvanrooyen@sun.ac.za
[3] Centre for Materials Engineering, University of Cape Town, South Africa, thorsten.becker@uct.ac.za

Abstract. Predicting and preventing stress induced support failure during laser powder bed fusion (LPBF) processing requires knowledge of the fracture toughness of the material in its as-built condition. When performing laboratory measurement of fracture toughness, large residual stresses that are present in the part due to the LPBF process can significantly affect the measurement and must be taken into consideration. In this article, fracture toughness in the as-built condition was measured to be 26 MPa.m$^{1/2}$ and the residual stress distribution in the crack plane was determined with simulation. Finally, the effective fracture toughness of the material was calculated, using the principle of superposition, to be ~ 47 MPa.m$^{1/2}$.

1 Introduction

Laser powder bed fusion (LPBF) is a high accuracy additive manufacturing technique capable of producing functional metal components out of any weldable metal, as reported by Wohlers *et al.* [1]. Ti6Al4V is of particular interest due to its excellent strength-to-weight ratio that can be maintained at high temperatures. To assist in the commercialisation of LPBF, it is important to improve our understanding of the physical phenomena that occur during the LPBF process. Large thermal gradients exist due to the relatively small weld-pool surrounded by solid material that is near room temperature. These thermal gradients cause thermal stresses that lead to distortion, the formation of residual stresses and can cause plastic deformation that may lead to the formation of cracks. Such cracks may lead to delamination of parts or failure of the support structures. The formation and growth of cracks at sharp corners can be investigated with fracture mechanics [2].

Therefore, the fracture toughness in the as-built condition of a material produced by LPBF provides information about its susceptibility to delamination and support failure and may be used to predict failure as shown by Tran *et al.* [3]. Kumar *et al.* [4] measured the fracture toughness (K_{IC}) of grade 23 Ti6Al4V produced by LPBF and subjected to a stress relief heat treatment to range between 48 and 58 MPa.m$^{1/2}$. In a similar study by Cain *et al.* [5] a substantially lower K_{IC}, between 16 and 28 MPa.m$^{1/2}$, was measured in a specimen that was

not stress relieved. The large difference between the two studies cannot conclusively be attributed to either residual stress or microstructure since a stress relief heat treatment can cause noticeable changes in microstructure.

Residual stress may aid or retard cracking, as argued by Becker *et al.* [6]. To determine its effect the level and distribution of residual stress must be known and the stress intensity factor due to residual stress (hereafter referred to as K_{Ires}) calculated. Vrancken *et al.* [7], showed that residual stresses in the crack plane of a compact tension specimen of Ti6Al4V produced by LPBF are close to the yield strength in some positions, tensile along the edges and compressive in the middle. They did not, however, calculate K_{Ires}. By measuring crack tip opening displacement of an unloaded compact tension specimen, Becker *et al.* [8] found that K_{Ires} is dependent on sample orientation and has a value of 5.2 MPa.m$^{1/2}$ when the crack plane is parallel to the base plate. Using a different technique to calculate K_{Ires}, O'Down *et al.* [9], measured residual stress distribution in welded ferritic steel with the help of neutron diffraction and showed that the stress intensity factor due to residual stress can be a significant percentage of the fracture toughness of the material.

All the above shows that when performing laboratory measurement of fracture toughness of a sample containing large residual stresses, it is important to quantify the effect of residual stress. In this article, the stress distribution on the crack plane of a compact tension specimen was calculated using simulation of the LPBF process. Thereafter, K_{Ires} was determined and added, using the super position principle, to the measured fracture toughness (K_{IC}) to calculate the effective fracture toughness (K_{effIC}) of the material without the influence of residual stress.

2 Experimental methods and simulations

2.1 Simulation of residual stress distribution

Simulation of the residual stress distribution was performed with the inherent strain method as described by Keller and Ploshikhin [10]. Simulation was performed in Simufact Additive 2020 with its built-in inherent strain method and material properties for Ti6Al4V. To improve the accuracy of the simulation three cantilevers were produced and the deflection thereof measured after the pillars were cut as illustrated in Fig. 1 (a). The deflection values were then used to calibrate the inherent strains with Simufact Additive 2020's built-in calibration procedure. The voxel size used for the calibration as well as the simulation was set to 0.25 mm.

The simulation used to determine the residual stress distribution included the machining steps of reducing the thickness of the block from 10 mm to 8 mm by removing 1 mm from each side and removing 2 mm from the top and bottom of the block. The wire-cutting step used to make the final shape was simplified as a straight cut up to the tip of the notch in the simulation.

2.2 Calculation of stress intensity factor due to residual stress (K_{Ires})

The residual stress distribution on the portion of the crack plane starting at the tip of the notch and extending 3.5 mm forward, which represents the residual stress where the pre-crack formed, was mapped to a model of the compact tension specimen in Abaqus CAE 2020. A grid was made to divide the 3.5 mm × 8 mm portion of the plane into 0.5 mm × 0.5 mm squares.

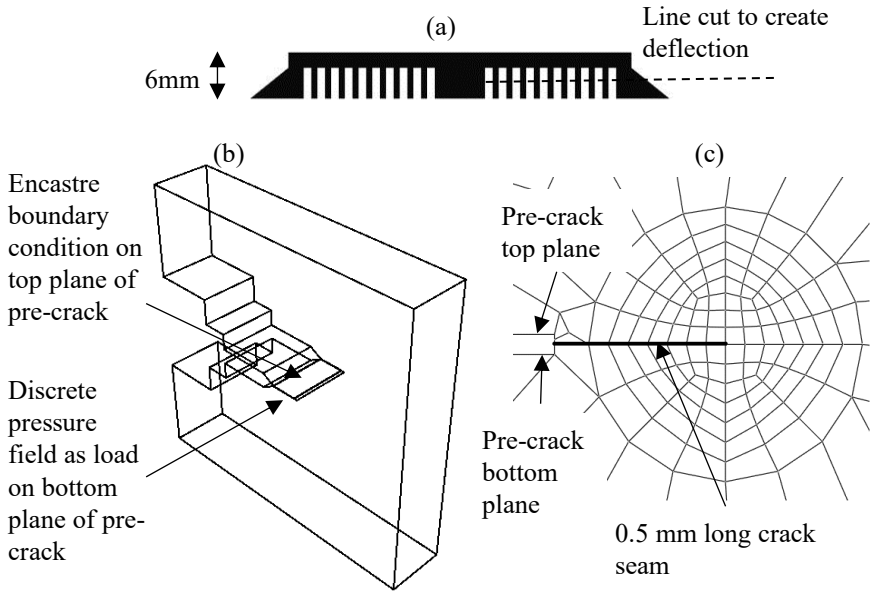

Fig. 1. (a) Schematic of cantilever used to calibrate inherent strains. (b) Geometry and boundary conditions used in Abaqus CAE 2020 to determine K_{Ires}. (c) Illustration of mesh around crack tip.

The residual stress in each square in the Simufact Additive 2020 simulation was set as a face pressure boundary condition on the element in the Abaqus CAE 2020 simulation corresponding to the same position on the bottom plane of the pre-crack of the compact tension specimen, see Fig. 1 (b). A tensile residual stress resulted in a force on the crack face that opens the crack and a compressive residual stress resulted in a force that closes the crack. The face-pressure boundary condition was not applied to the elements closer than 0.5 mm to the crack tip so that a crack-seam could be assigned to this portion of the pre-crack. See illustration in Fig. 1 (c).

In the Abaqus CAE 2020 simulation the material was chosen to be linear elastic with a Young's modulus (E) of 120 GPa and a Poisson's ratio(v) of 0.32. The top plane of the pre-crack was kept in place with an encastre boundary condition. The stress intensity factor due to residual stress was then be calculated in a similar manner to O'Down *et al.* [9]. To extract K_{Ires} the built-in crack feature of Abaqus CAE 2020 was used. The calculation method was set to be based on a J-integral with four contours. To assist contour calculations a spiderweb shaped mesh was made around the crack tip as illustrated in Fig. 1 (c). The energy release rate (G), which is equal to the J-integral for a linear elastic material, was converted to stress intensity factor using $K = \sqrt{EG/(1-\nu^2)}$ for plane strain conditions.

2.3 Specimen fabrication, fracture toughness testing and fractography

The material used in this study was manufactured as three rectangular blocks out of EOS grade 23 Ti6Al4V powder on an EOS M290 LPBF machine. Compact tension specimens required for fracture toughness testing was cut out of the rectangular blocks, see Fig. 2 (a). Care was taken to ensure that the position of the specimen as it was cut out of the block was known so that machining could be included in the simulation of residual stress.

Specimens were tested in the as-built condition. A specimen width (W) of 32 mm and thickness (B) of 8 mm was used, all other dimensions were chosen according to ASTM E1820 [11]. K_{IC} measurements were done on specimens pre-cracked to a total crack length (a) of

approximately 16 mm corresponding to $a/W \approx 0.5$. The pre-crack extended 4 mm from the tip of the starter notch. Thereafter, it was quasi-statically loaded to failure while measuring load and crack mouth opening displacement. After testing the length of the pre-crack was measured with a traveling microscope so that K_{IC} could be determined as per ASTM E1820. The samples were tested in the *Z-X* orientation, meaning the load was applied parallel to the *Z*-axis and the crack propagated along the *X*-axis. Photos of the pre-crack was taken with a stereo microscope so that its shape can be compared to the residual stress distributions.

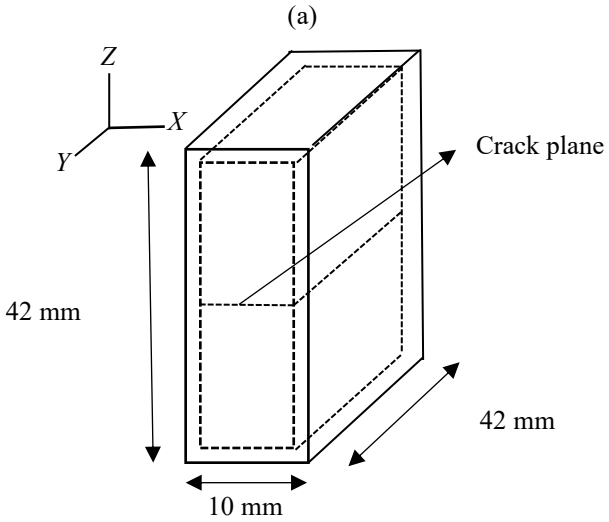

Fig. 2. (a) Orientation of manufactured blocks (solid lines) and compact tension specimens (dotted lines). Coordinate system is in accordance with ASTM F2924-14 [12].

During a fracture toughness test performed on a sample containing large residual stresses, the effective stress intensity factor is, according to the superposition principle, the sum of the applied stress intensity factor and K_{Ires}. Therefore, $K_{effIC} = K_{IC} + K_{Ires}$.

3 Results

The measured deflections of the cantilevers used for the calibration of inherent strains were 0.39 mm, 0.48 mm, and 0.52 mm. The average of the three measurements was used for the calibration. The variability between the three measurements may be due to accuracy of the measurement technique. The computed calibrated inherent strains were ε_x = -0.0041, ε_y = -0.0041 and ε_z = -0.031. The distribution of the normal stress on the crack plane is shown in Fig. 3 (a). The position of the pre-crack is also shown. Note that the stress is tensile along the sides of the sample and compressive in the middle. High stresses are seen at the tip of the notch and a small compressive zone is seen in the middle of the pre-crack front. Photos of the pre-crack in the as-built conditions is shown in Fig. 3 (b). Faster crack growth is seen on the sides of the pre-crack in Fig. 3 (b) which corresponds to the larger tensile residual stress along the sides as seen in Fig. 3 (a).

K_{IC} of the as-built specimens are shown in Table 1. Note that the three repeat measurements do not differ more than 1 % from the average. Furthermore, it is seen that K_{Ires}, also shown in Table 1, is a significant fraction (45 %) of K_{effIC}. When analysing the results, it is important to keep in mind that K_{Ires} calculated by the different contours used for the *J*-integral ranged between 18.6 MPa.m$^{1/2}$ and 23.1 MPa.m$^{1/2}$. K_{Ires} reported in Table 1 is the average of that calculated from the four contours.

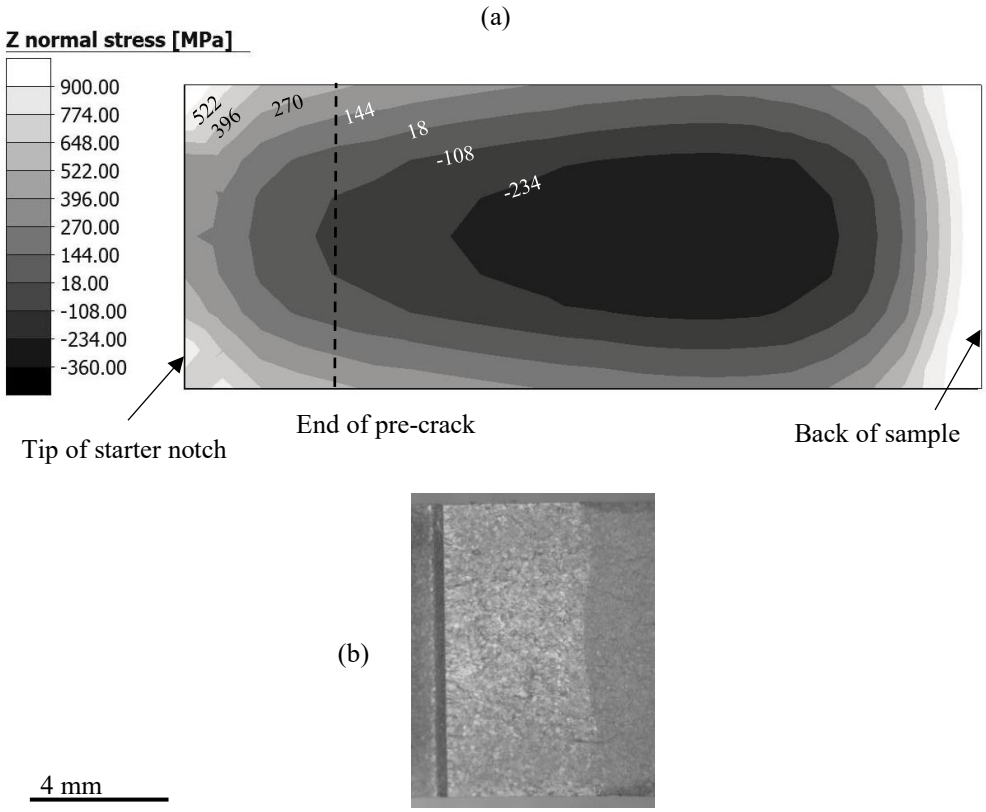

Fig. 3. (a) Simulated distribution of normal stress in *Z*-direction on crack plane. (b) Photo of pre-crack in as-built *Z-X* sample.

4 Discussion

The calibration procedure in Simufact Additive 2020 resulted in negative inherent strain values in all three directions. This observation agrees with both mechanisms of residual stress formation described by Mercelis and Kruth, [13]. Furthermore, the simulated residual stress distribution, consisting of compressive residual stresses in the middle and tensile residual stresses along the edges on the crack plane as illustrated in Fig. 3 (a), agrees well with experimental measurements of residual stress done by researchers who considered similar geometries [14, 7, 8].To understand how such stresses form one can visualize that when the top layer shrinks it attempts to curl the edges upward, but the edges are constrained by the layers and baseplate beneath it which causes tensile residual stresses along the edges. Similarly, the middle of the shrinking top layer attempts to bend downward but is constrained by the layers and base plate beneath it resulting in compressive residual stress in the middle.

The effect of the residual stress distribution is clearly visible from the shape of the pre-crack. In a residual stress-free compact tension specimen, the pre-crack grows faster in the centre because a plane strain condition exists here while the sides experience plane stress. The faster growth of the pre-crack on the edges in the current specimen, as seen in Fig. 3 (b), corresponds to the larger tensile residual stresses in this region. Looking at the results quantitatively, it is seen that K_{Ires} is ~ 45 % of $K_{effIC.,}$ meaning residual stress had a substantial effect on fracture behaviour.

Table 1. Fracture toughness measurements and stress intensity factor due to residual stress

Condition and orientation	Repeat	K_{IC} (MPa.m$^{1/2}$)	K_{Ires} (MPa.m$^{1/2}$)	K_{effIC} (MPa.m$^{1/2}$)
As-built Z-X	1	25.6	21.3	46.9
As-built Z-X	2	25.5	21.3	46.8
As-built Z-X	3	25.2	21.3	46.5

Furthermore, the effective fracture toughness of 47 MPa.m$^{1/2}$ is slightly lower than the 48 – 58 MPa.m$^{1/2}$ K_{IC} values reported after a stress relief heat treatment by Upadrasta *et al.* [4]. This suggests that the difference between K_{IC} in this study and that reported by Upadrasta *et al.* [4] is due to residual stress instead of microstructural changes caused by the stress relief heat treatment. Looking at estimates of K_{Ires} available in literature it is seen that K_{Ires} is much larger than what was observed by Becker *et al.* [8]. Differences in the length of the pre-crack, the geometry of the specimen or the machining procedure can cause variations in the residual stress distribution which might be the reason. K_{IC} measured in the as-built condition is approximately 60 % higher than what was measured by Cain *et al.* [5] for a compact tension specimen produced in the same orientation and in the same condition. Again, the difference may be due the residual stress distribution caused by different sample thicknesses and machining procedures.

5 Conclusions

Based on the results obtained the following conclusions can be drawn:

- The distribution of residual stress determined with Simufact Additive 2020 qualitatively agrees with experimental data
- The K_{effIC} of as-built Ti6Al4V in the *Z-X* orientation produced with the process parameters used in this paper is 47 MPa.m$^{1/2}$ which is substantially higher than K_{IC} measured in this condition and shows the importance of taking residual stress into consideration when measuring as-built fracture toughness
- Future work is needed to experimentally verify the stress intensity factor due to residual stress

Acknowledgements - Funding provided by the South African Council for Scientific and Industrial Research through the Aeroswift project is acknowledged. Cantilever data provided by Dean-Paul Kouprianoff from the Central University of Technology is acknowledged.

References

[1] T. T. Wohlers, I. Campbell, T. Caffrey, O. Diegel, and J. Kowen, "Wohlers Report 2018: 3D Printing and Additive Manufacturing State of the Industry: Annual World Wide Progress Report," 2018.

[2] T.L. Anderson, *Fracture Mechanics Fundamentals and Applications*, Fourth. New York: CRC Press Taylor & Francis Group, 2017.

[3] H. T. Tran, Q. Chen, J. Mohan, and A. C. To, "A new method for predicting cracking at the interface between solid and lattice support during laser powder bed fusion additive manufacturing," *Additive Manufacturing*, 2020, doi: 10.1016/j.addma.2020.101050.

[4] P. Kumar, O. Prakash, and U. Ramamurty, "Micro-and meso-structures and their influence on mechanical properties of selectively laser melted Ti-6Al-4V," *Acta Materialia*, vol. 154, pp. 246–260, Aug. 2018, doi: 10.1016/j.actamat.2018.05.044.

[5] V. Cain, L. Thijs, J. van Humbeeck, B. van Hooreweder, and R. Knutsen, "Crack propagation and fracture toughness of Ti6Al4V alloy produced by selective laser melting," *Additive Manufacturing*, vol. 5, pp. 68–76, Jan. 2015, doi: 10.1016/J.ADDMA.2014.12.006.

[6] T. H. Becker, P. Kumar, and U. Ramamurty, "Fracture and fatigue in additively manufactured metals," *Acta Materialia*, vol. 219, p. 117240, Oct. 2021, doi: 10.1016/J.ACTAMAT.2021.117240.

[7] B. Vrancken, V. Cain, R. Knutsen, and J. van Humbeeck, "Residual stress via the contour method in compact tension specimens produced via selective laser melting," *Scripta Materialia*, vol. 87, pp. 29–32, Sep. 2014, doi: 10.1016/j.scriptamat.2014.05.016.

[8] T. H. Becker, N. M. Dhansay, G. M. ter Haar, and K. Vanmeensel, "Near-threshold fatigue crack growth rates of laser powder bed fusion produced Ti-Aal-4V," *Acta Materialia*, vol. 197, pp. 269–282, 2020, doi: 10.1016/j.actamat.2020.07.049.

[9] N. P. O'Dowd, K. M. Nikbin, H. Y. Lee, R. C. Wimpory, and F. R. Biglari, "Stress intensity factors due to residual stresses in T-plate welds," *Journal of Pressure Vessel Technology, Transactions of the ASME*, vol. 126, no. 4, pp. 432–437, 2004, doi: 10.1115/1.1804199.

[10] N. Keller and V. Ploshikhin, "New method for fast predictions of residual stress and distortion of AM parts." Accessed: Jul. 17, 2019. [Online]. Available: https://pdfs.semanticscholar.org/6c4c/ad8045bdaac3d47b9c63ddef3a81c510d28a.pdf

[11] "ASTM E1820-01 Standard test method for measurement of fracture toughness." ASTM International, 2001.

[12] "ASTM F2924-4 Standard Specification for Additive Manufacturing Titanium-6 Aluminum-4 Vanadium with Powder Bed Fusion." ASTM International, 2014.

[13] P. Mercelis and J. Kruth, "Residual stresses in selective laser sintering and selective laser melting," *Rapid Prototyping Journal*, vol. 12, no. 5, pp. 254–265, Oct. 2006, doi: 10.1108/13552540610707013.

[14] L. S. Anderson, A. M. Venter, B. Vrancken, D. Marais, J. van Humbeeck, and T. H. Becker, "Investigating the Residual Stress Distribution in Selective Laser Melting Produced Ti-6Al-4V using Neutron Diffraction," *Materials Research Forum LLC Materials Research Proceedings*, vol. 4, pp. 73–78, 2017, doi: 10.21741/9781945291678-11.